NJC

PAPER

View Article Online
View Journal | View Issue

Cite this: *New J. Chem.*, 2015, 39, 6040

High photoconductive combustion synthesized TiO_2 derived nanobelts for photocatalytic water purification under solar irradiation

Neerugatti KrishnaRao Eswar,[a] Praveen Chandrashekarapura Ramamurthy[ab] and Giridhar Madras*[c]

Received (in Montpellier, France) 22nd April 2015,
Accepted 29th May 2015

DOI: 10.1039/c5nj01001b

www.rsc.org/njc

Drinking water scarcity is a major issue that needs to be addressed seriously. Water needs to be purified from organic pollutants and bacterial contamination. In this study, sunlight driven photocatalysis for the degradation of dyes and bacterial inactivation has been conducted over TiO_2 nanoparticles (CST) and TiO_2 nanobelts (CSTNB). TiO_2 nanoparticles were synthesized by a solution combustion process using ascorbic acid as a fuel. Acid etched TiO_2 nanobelts (CSTNB) were synthesized using combustion synthesized TiO_2 as a novel precursor. The mechanism of formation of TiO_2 nanobelts was hypothesized. The antibacterial activity of combustion synthesized TiO_2 and acid etched TiO_2 nanobelts were evaluated against *Escherichia coli* and compared against commercial TiO_2. Various characterization studies like X-ray diffraction analysis, BET surface area analysis, diffused reflectance measurements were performed. Microscopic structures and high resolution images were analyzed using scanning electron microscopy, transmission electron microscopy. The extent of photo-stability and reusability of the catalyst was evaluated by conducting repeated cycles of photo degradation experiments and was compared to the commercial grade TiO_2. The reactive radical species responsible for high photocatalytic and antibacterial activity has been determined by performing multiple scavenger reactions. The excellent charge transfer mechanism, high generation of hydroxyl and hole radicals resulted in enhanced photocatalytic activity of the acid etched TiO_2 nanobelts compared to commercial TiO_2 and nanobelts made from commercial TiO_2.

1. Introduction

Recent human activities have drastically increased environmental pollution, which exhibits a negative impact on clean water availability. The release of toxic wastes into rivers and streams not only increases the demand for clean water but also for sustainable technology for water purification. Water-borne epidemics still occur in many parts of the world.[1] Various filtration and disinfection technologies are available to provide clean water; however, they also have several disadvantages. Conventional water disinfection systems such as chlorination *etc.* produce hazardous disinfection byproducts. The microbes also tend to develop resistance towards these disinfection methods. Water purification systems such as adsorption and filtration do not result in the destruction of these pollutants. Therefore, studies are focused on advanced oxidation processes as an alternative water treatment technique to purify polluted water. The advanced oxidation process is basically generation of highly reactive radical species that subsequently results in the degradation of organic pollutants.[2]

Due to the rapid growth of nanotechnology, several nanomaterials are engineered for these advanced oxidation processes including microbial disinfection.[3] Among them, TiO_2 is used widely because of its abundance and non-toxicity. TiO_2 has been widely tested for its activity against a variety of pathogens[4] and towards organic contaminants.[5,6] In addition to TiO_2, titanium phosphates have also been used for catalytic degradation of dyes and organic compounds.[7,8] Various methods such as aerosol,[9] hydrothermal,[10,11] inert-gas condensation[12] and sol–gel[13] have been used to synthesize TiO_2. However, all these techniques have their limitations. TiO_2 synthesized using the aerosol method tends to aggregate because of high temperature, while TiO_2 synthesized using the sol–gel technique requires utilization of multiple solvents with many laborious steps. TiO_2 synthesized by the inert gas condensation technique requires high vacuum which makes the technique much costlier. The synthesis by the hydrothermal method requires several post synthesis processing steps that make the technique difficult.

[a] *Centre for Nanoscience and Engineering, Indian Institute of Science, Bangalore-560012, India*
[b] *Department of Materials Engineering, Indian Institute of Science, Bangalore-560012, India*
[c] *Department of Chemical Engineering, Indian Institute of Science, Bangalore-560012, India. E-mail: giridhar@chemeng.iisc.ernet.in; Fax: +91 80 23600683; Tel: +91 80 22932321*

The synthesis of TiO_2 using a solution combustion method is easier, faster and efficient compared to other methods[14,15] offering nanoparticles with lower band gap and high activity towards degradation of organic contaminants and killing pathogens.[16] Though there are various techniques to synthesize TiO_2, its properties depend on crystal structure, size, dimension and morphology.[17] Photocatalysis of organic contaminants using natural sunlight[8,18,19] rather than artificially powered lights have more advantage in reducing the cost, process and also utilizing both visible and ultraviolet regions of the light spectrum. Many recent reports on extending the absorption of light towards the visible region using the catalysts have shown promising results.[20–25] If there is no significant visible light absorption, increasing the photoactivity by just controlling the morphological features can also be given equal importance. Considering various morphologies, the nanobelt structure of TiO_2 is of great interest for photocatalysis.[26,27] These nanobelts are synthesized by reacting TiO_2 with a high alkaline solution at low temperature and high pressure. These nanobelt structures are utilized as substrates for making heterostructures combined with other oxides in order to engineer its bandgap and increase the activity.[28,29] Besides photocatalysis, these nanobelt structures of TiO_2 have been used for developing sensors and antibacterial applications.[30,31]

In this report, we have prepared TiO_2 by a solution combustion method using ascorbic acid as a fuel. To the best of our knowledge, this is a novel study to report combustion synthesis using ascorbic acid as a reducer and synthesis of TiO_2 nanobelts using combustion synthesized TiO_2 as a precursor. The photocatalytic activities of the two compounds synthesized have been evaluated by degrading dyes and evaluating their antibacterial activity. The degradation and antibacterial properties of combustion synthesized TiO_2 and combustion synthesized TiO_2 derived nanobelts have been compared with commercial TiO_2 (Degussa-P25) and nanobelts synthesized from commercial TiO_2.

2. Experimental

2.1. Materials

Titanium iso-propoxide (>97% purity) was purchased from Sigma-Aldrich (USA). L-Ascorbic acid-LR, methylene blue, methyl orange were purchased from SD fine chemicals Ltd. (India). Commercial TiO_2 was obtained from Evonik. Sodium hydroxide, sulphuric acid (98%), hydrochloric acid (35%) and nitric acid (69%) were purchased from Merck (India). Luria nutrient broth and nutrient agar were purchased from Hi Media (India). Double distilled Millipore water was used for all the experiments.

2.2. Catalyst synthesis

2.2.1. TiO_2 synthesis by the solution combustion process. Combustion synthesized TiO_2 (CST) was prepared according to the reports[14] with a modification in the choice of fuel. Initially, titanium iso-propoxide was dissolved in ice-cold water to get a white precipitate which is $TiO(OH)_2$. 1 : 2 nitric acid (by volume) was used to dissolve the white precipitate to obtain a transparent solution of titanyl nitrate. A known concentration of titanyl nitrate was mixed with a stoichiometric amount of L-ascorbic acid to maintain an equal molar ratio of oxidizer to fuel. The combustion reaction is as follows:

$$2TiO(NO_3)_2 + C_6H_8O_6 \xrightarrow{350\,^{\circ}C} 2TiO_2 + 6CO_2 + 4H_2O + 2N_2 \quad (1)$$

A smoldering type of combustion occurred when the combustion mixture was kept at 350 °C in a preheated furnace for 15 min. The resultant product was ground finely using a mortar and pestle to obtain a pale yellow colored powder.

2.2.2. Synthesis of TiO_2 nanobelts from combustion synthesized TiO_2. TiO_2 nanobelts (CSTNB) from combustion synthesized TiO_2 (CST) were prepared according to the report.[32] 0.1 g of CST was dispersed in 20 ml of 10 M sodium hydroxide solution. The mixture was stirred vigorously and transferred into a Teflon coated steel autoclave, heated at 180 °C for 48 h to obtain $Na_2Ti_3O_7$. The resultant powder was washed with de-ionized water several times and then dispersed in 0.1 M HCl for 24 h. This was further washed with de-ionized water until the pH of the washed solution becomes 7 to obtain $H_2Ti_3O_7$. The resultant hydrogen titanate belts were added to 0.02 M sulphuric acid filled up to 80% of the Teflon coated steel autoclave, heated at 100 °C for 12 h to obtain acid etched hydrogen titanate belts. The product obtained was washed several times with de-ionized water and then maintained at 70 °C for 10 h. The obtained powder was annealed at 600 °C in a muffle furnace for 2 h to obtain acid etched TiO_2 nanobelts. A similar procedure was followed for the synthesis of nanobelts from commercial TiO_2.

2.3. Catalyst characterization

X-ray diffraction spectra were obtained using a Rigaku diffractometer using Cu-Kα radiation with a scan rate of 1° min^{-1} in the 10°–80° scan range. Scanning electron microscopic images were captured using ULTRA55 FESEM, Carl Zeiss. Catalyst particles were dispersed in absolute ethanol and sonicated for 10 min. These dispersed samples were drop-casted on silica wafers which were stuck to carbon tape on a SEM aluminium stub. Prepared samples were kept under vacuum for 12 h; samples were gold sputtered using Quorum sputtering before imaging. Transmission electron microscopic pictures were acquired using Tecnai T20 operated at 180 kV. Samples for TEM analysis were prepared by dispersing particles in iso-propanol and ultrasonicated for 10 min before drop casting on copper grids.

The grids were maintained under vacuum for 24 h before subjecting them for imaging. Band gap measurements were done using a solid state UV-visible spectrophotometer (Perkin Elmer, Lambda 35). Absorbance measurements for photocatalysis experiments were analyzed using a UV-visible spectrophotometer (Shimadzu-UV 1700). Catalyst particles were regenerated at 120 °C for 2 h for BET surface analysis using Nova-1000 Quantachrome. The photoconductivity experiments were carried out using ITO coated electrode substrates and a class 3A solar simulator. The solar simulator consists of a 450 W xenon lamp with an

Oriel Sol 1.5 air filter. The catalyst samples were drop casted between ITO electrodes.

2.4. Photocatalysis

2.4.1. Photochemical reactor. As a preliminary experiment, initially the catalysts were used to perform degradation of methyl orange in the presence of 125 W mercury vapor lamp (λ_{max} = 365 nm). Unless stated otherwise, all of the photocatalytic and antibacterial experiments were carried out in 100 ml quartz reactors under solar light. All the experiments were conducted under direct sunlight between 11:00 am and 2:00 pm, when the solar intensity fluctuations are minimal and the intensity was ~975 W m^{-2}. The reaction mixture was stirred vigorously using a magnetic stirrer and samples were taken from the reactor at specific intervals for absorbance measurements. Control experiments were done in the dark to measure the adsorption of the dye over catalyst particles.

2.4.2. Dye degradation. Photocatalysis was carried out using 10 ppm aqueous solution of methylene blue and methyl orange. The catalyst concentration was maintained as 1 g l^{-1} for all the experiments. Initially, all the catalyst particles were suspended in the dye solution and kept in the dark for 2 h in order to achieve stable absorption–desorption equilibrium. At regular intervals, samples were collected from the reactor and centrifuged at 5000 rpm for 5 min to separate catalyst particles from the solution and subjected to absorbance measurements using a UV-visible spectrophotometer. All the solar experiments were repeated three times unless stated otherwise.

2.4.3. Antibacterial evaluation. A bacterial culture of wild type *Escherichia coli* was prepared using a liquid nutrient broth. Before that, the liquid nutrient broth, nutrient agar solutions and all other accessories such as L-rods, Petri plates, micro tips *etc.* were autoclaved. Initially, the bacterial culture was subjected to centrifugation at 5000 rpm for 10 min to separate bacterial cells as a pellet. The pellet was re-suspended in a phosphate buffer saline (PBS) solution in order to maintain the concentration of the bacteria. Similarly, an autoclaved nutrient agar solution was poured equally in all Petri plates and kept for some time inside the laminar hood for solidification. Dark experiments were conducted with 0.25 g l^{-1} catalyst and bacterial culture alone without keeping the reactor under solar irradiation. Later, catalyst particles were added into a fresh bacterial suspension and subjected to solar radiation. To measure the antibacterial activity, aliquots of suspensions were taken at specific intervals. 100 μl of serially diluted aliquots were spread onto nutrient agar plates that were prepared already and incubated at 37 °C overnight. The experiment was further repeated and the bacterial colonies grown on the agar plates were counted and then evaluated.

3. Result and discussion

3.1. Characterization

The powder X-ray diffraction pattern of combustion synthesized TiO_2 and acid etched TiO_2 nanobelts is shown in Fig. 1(a) and (b). The rutile phase at a 2θ value of 27° in the pattern was

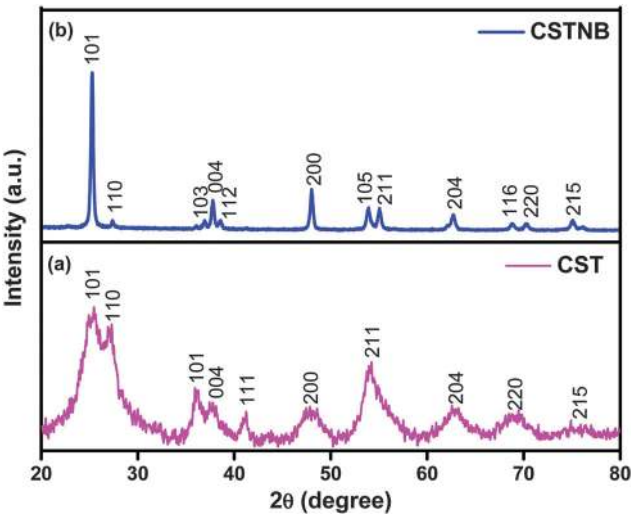

Fig. 1 X-ray diffraction patterns of combustion synthesized TiO_2 and acid etched TiO_2 nanobelts.

observed besides a predominant anatase phase (JCPDS No: 00-004-0477) at a 2θ value of 25.4° with (101) as $\langle hkl \rangle$ parameters. It is known that low temperature combustion synthesis of TiO_2 results in the formation of pure anatase phase.[14,15] However, the synthesized product with ascorbic acid as a fuel has shown the possibility of formation of a rutile phase that has been noticed at a 2θ value of 36.0° and 54.2° (JCPDS No: 00-001-1292). It has been reported that TiO_2 synthesized using titanyl nitrate and ascorbic acid in 5 : 3 molar ratio resulted in a pure anatase phase.[33] However, if the stoichiometric ratio becomes 2 : 1, the rutile phase co-exists with anatase.

The X-ray diffraction pattern of acid etched TiO_2 nanobelts shows a huge peak that corresponds to anatase (JCPDS No: 00-004-0477) and also a small adjacent peak at 27.6° corresponding to rutile (JCPDS No: 00-001-1292).

UV-vis diffuse reflectance spectra of combustion synthesized TiO_2 and acid etched TiO_2 nanobelts are shown in Fig. 2. The combustion

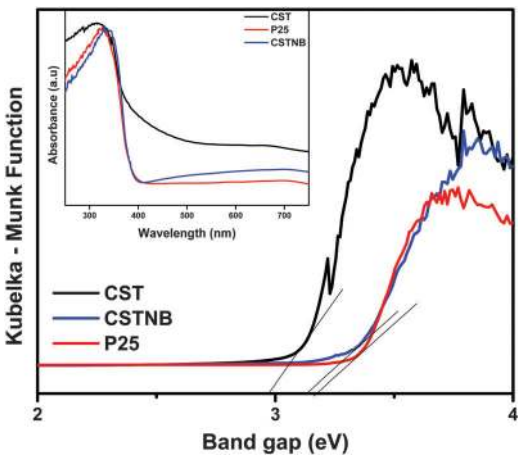

Fig. 2 Diffused reflectance spectra of combustion synthesized TiO_2 (CST), acid etched TiO_2 nanobelts (CTSNB) and Degussa P-25, inset shows the absorbance spectra.

synthesized TiO_2 shows significant absorption at 400–500 nm. The band gap of combustion synthesized TiO_2 is lower compared to the other two catalysts because the combustion synthesis involves generation of adventitious carbon to the TiO_2 and hence that red shifts the absorption spectra of light.[14] The band gap was calculated using the Kubelka–Munk equation and was found to be 2.98 eV, 3.13 eV and 3.20 eV for combustion synthesized TiO_2, acid etched TiO_2 nanobelts and commercial grade TiO_2 Degussa P-25 respectively. Since the catalysts show a strong absorption in the UV region, utilization of natural solar energy is also feasible rather than experimenting photocatalysis under an artificial UV source.

The mechanism of formation of partially etched TiO_2 nanobelts can be proposed as follows. When the TiO_2 precursor is reacted with high caustic concentration, Ti–O–Ti bonds would break and again reassemble through edges.[34] Later, the Ti–O–Ti bond becomes Ti–O–Na bonds. Many such units assemble together and form dimers. These dimers condense with each other and form belt like structures.[35,36] During an ion exchange reaction between the layered sheets of sodium titanates and hydrochloric acid, sodium titanate is converted into hydrogen titanate. Corrugated or etched structures of these belts were obtained by reacting hydrogen titanate under acid hydrothermal conditions. The protionic species in sulphuric acid reacts with the hydrogen titanate belt structure to form Ti^{4+} ions in the reaction mixture. These ions tend to get hydrolyzed on the surface of existing belt structures through heterogeneous nucleation resulting in the formation of a large number of etched surfaces.[29] Since combustion synthesized TiO_2 is used as a precursor for the first time, we hypothesize that the raw material has been partially etched causing some of the belts to get etched completely forming bits and pieces of TiO_2 islands leaving behind etched surfaces as shown in Fig. 3.

The scanning electron microscopic images show pristine hydrogen titanate belts with many inherent voids. Fig. 4(a) and (b) shows a wide distribution of nanobelts and the particle islands on top of them. The combustion synthesized TiO_2 nanoparticles are 10–15 nm in size and spherical in shape. The size of the TiO_2 nanobelts was found to be in the range of 100–300 nm. The surface area for combustion synthesized TiO_2 and titanate nanobelts were found to be 120 $m^2\ g^{-1}$ and 35 $m^2\ g^{-1}$ respectively. Though a number of voids have formed in the belt structure, there was no significant increase in the surface area of the nanobelts. However, after the acid etching process, the surface area of TiO_2 nanobelts increased to 72 $m^2\ g^{-1}$. After acid etching, several TiO_2 islands and separate particles formed on the existing belt structures and on the partially etched structures; this could have contributed to the increase in surface area.[29]

The transmission electron microscopic image of acid etched TiO_2 nanobelts (Fig. 5b) shows the presence of oxidation induced void formation. The *d*-spacing of the rutile phase was not clearly distinguishable whereas it was found to be 0.35 nm for combustion synthesized TiO_2 and acid etched TiO_2 nanobelts.

The particle size of combustion synthesized TiO_2 is very small and highly nanocrystalline compared to that of P25. It also consists of a lot of adventitious carbon. From the X-ray diffraction pattern,

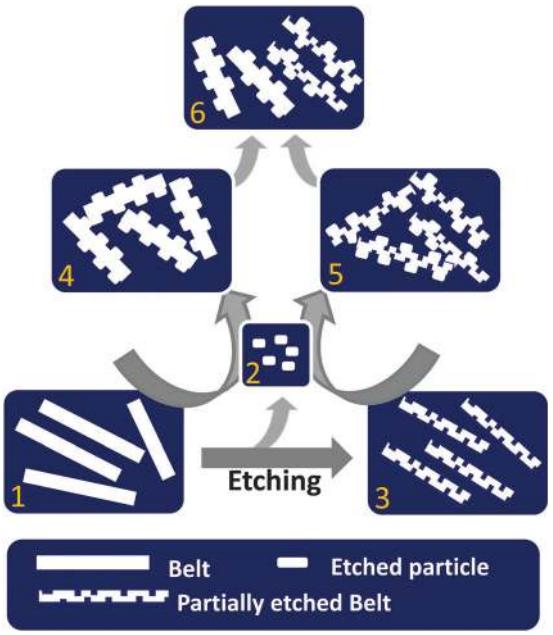

Fig. 3 Schematic of the mechanism of formation of partially etched TiO_2 nanobelts. Nanobelts (1) are etched to form particles (2) and etched belts (3). The particles on the nanobelt lead to formation of (4) and particles on etched nanobelts to (5). The final product (6) consists of both (4) and (5).

the combustion synthesized TiO_2, using ascorbic acid as a fuel, consists almost equal composition of anatase and rutile. Similarly, the surface area of combustion synthesized TiO_2 is very high compared to that of P25 because of its high porous nature. Therefore, the structural and morphological properties of the nanobelts vary significantly with respect to change in precursor TiO_2.[37] Due to the above reasons, combustion synthesized TiO_2 developed many defects which became further easier to form unique multiple etched TiO_2 islands during acid hydrothermal treatment. Hence, it can be proposed that utilizing highly porous combustion synthesized TiO_2 instead of commercial P25 results in the development of high photoactive TiO_2 nanobelts.

The photoluminescence spectra for combustion synthesized TiO_2 and acid etched nanobelts are shown in Fig. 6. The photoluminescence spectra were recorded by exciting the sample at 325 nm. The combustion synthesized TiO_2 exhibited high PL intensity compared to the TiO_2 nanobelts. Basically, the photoluminescence emission of anatase TiO_2 might be due to different reasons such as surface states,[38] presence of oxygen vacancies[39] and self-trapped excitons.[40] However, the combustion synthesized TiO_2 exhibits both anatase and rutile phases. The recorded PL spectra could arise from both anatase and rutile properties of TiO_2. The emission at 425 nm can correspond to intrinsic states of TiO_2 which is close to 412 nm[41] and not surface states. The peak at 525 nm can be correlated to oxygen vacancies.[39,42] Oxygen vacancies tend to be helpful in the photocatalytic dye degradation process. However, oxygen vacancies on the (110) rutile phase of TiO_2 have been shown to exhibit an inhibitive effect on the photocatalytic effect. The unpaired electrons at the oxygen vacancy sites tend to combine with the photo-excited holes at the surface.[43] Hence,

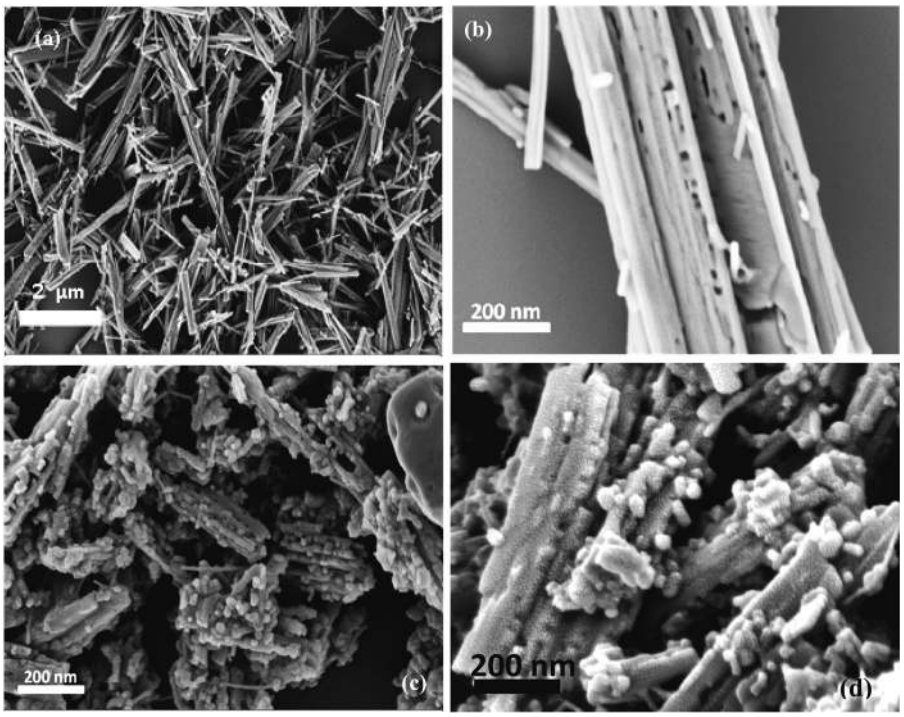

Fig. 4 Scanning electron microscopic images of (a) and (b) pristine nanobelts and (c) and (d) acid etched TiO_2 nanobelts.

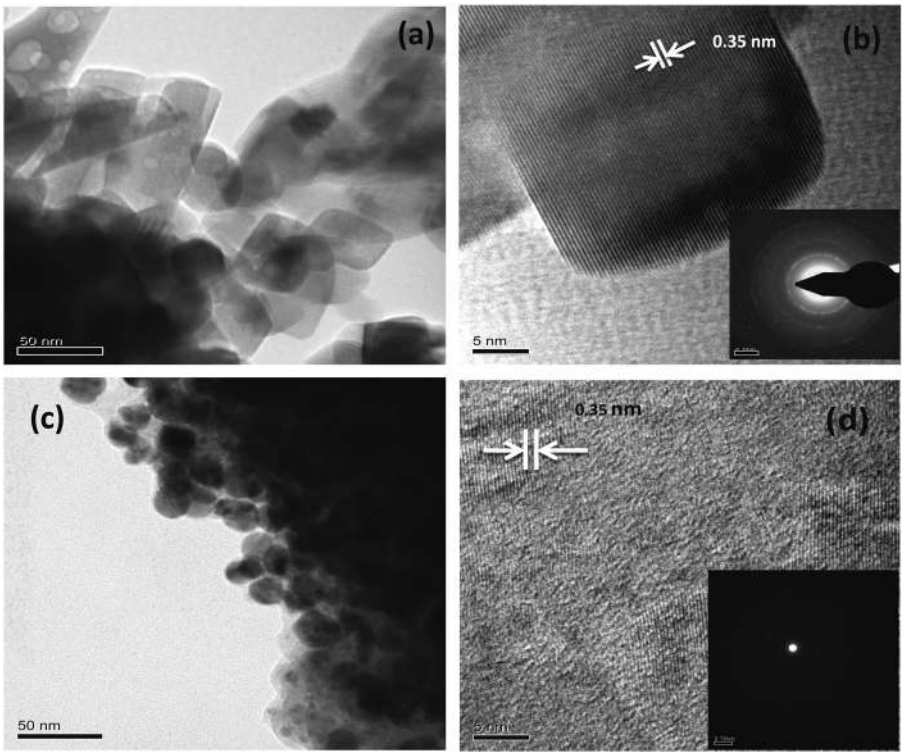

Fig. 5 Bright field TEM image of (a) acid etched TiO_2 nanobelts and (c) combustion synthesized TiO_2, HRTEM image of (b) acid etched TiO_2 nanobelts and (d) combustion synthesized TiO_2 (inset shows the selected area diffraction pattern).

combustion synthesized TiO_2 has many oxygen vacancies but also it consists of a significant rutile phase which could probably lead to a high intensity of photoluminescence. However, the photoluminescence intensity was less for acid etched TiO_2 nanobelts suggesting that a higher recombination occurred for combustion synthesized TiO_2 and it is prevented

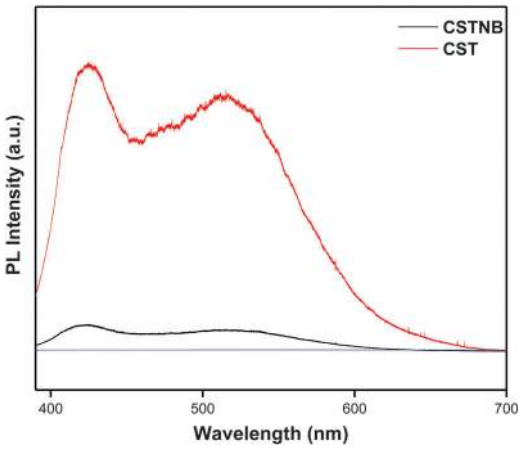

Fig. 6 Photoluminescence spectra of combustion synthesized TiO_2 and acid etched TiO_2 nanobelts.

in acid etched TiO_2 nanobelts, which is also supported by photo-conductivity analysis.

The intensity of electron counts with respect to binding energy was plotted for carbon, oxygen and titanium elements using X-ray photoelectron spectroscopy analysis. Fig. 7(a) and (b) show the XPS spectra for Ti-2p of TiO_2 nanobelts and combustion synthesized TiO_2 respectively. The peak at 458.7 eV and 457.7 eV ($2p_{3/2}$) corresponds to the Ti^{4+} and Ti^{3+} state of TiO_2 respectively. The Ti-2p XPS spectra of combustion synthesized TiO_2, as shown in Fig. 7(b), exhibits Ti in +3 state at 458.2 eV, and in +4 state at 459.2 eV.[44]

Fig. 7(c) and (d) shows the XPS peaks of O 1s of combustion synthesized TiO_2 and TiO_2 nanobelts. Both the spectra consist of peaks corresponding to lattice oxygen near 530 eV.[45,46] Besides lattice oxygen, oxygen vacancies and chemisorbed or dissociated oxygen species can also be observed in the O 1s profile of metal oxides.[47,48] The surface hydroxyl groups in combustion synthesized TiO_2[14] would very much likely contribute to the excellent photoactivity despite the fact that most of the photo-excited holes are recombining at the surface. Similarly, chemisorbed or dissociated oxygen species in TiO_2 nanobelts could also contribute in direct participation of photocatalysis by generating superoxide radical species, which can also be seen from scavenger experiments. Hence, it shows significant photoactivity similar to commercial TiO_2.

Conductivity studies were carried out to measure the photocurrent generated during the experiment. The photocurrent was measured at 0 V and by radiating the light from a solar simulator using a 2420 Keithley source meter. Fig. 8 shows the photocurrent measured with respect to the on and off switch

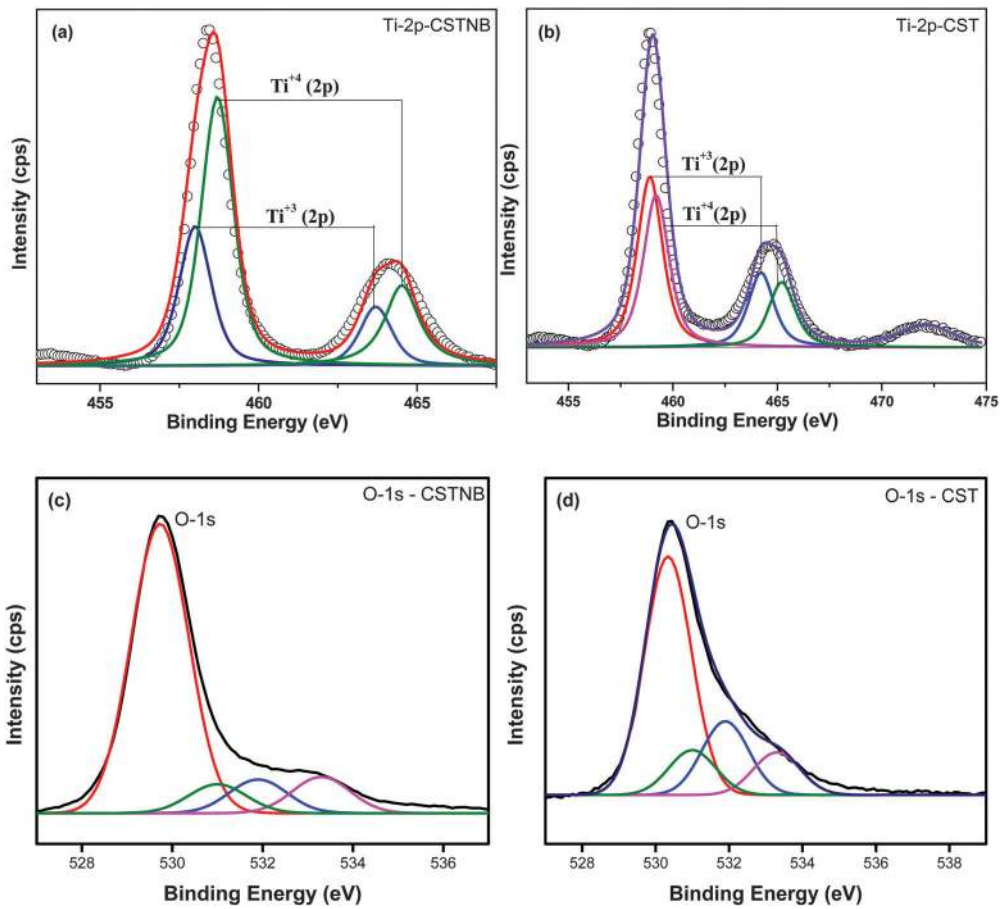

Fig. 7 X-ray photoelectron spectra of Ti-2p for (a) acid etched TiO_2 nanobelts and (b) combustion synthesized TiO_2. X-ray photoelectron spectra of O-1s for (c) acid etched TiO_2 nanobelts and (d) combustion synthesized TiO_2.

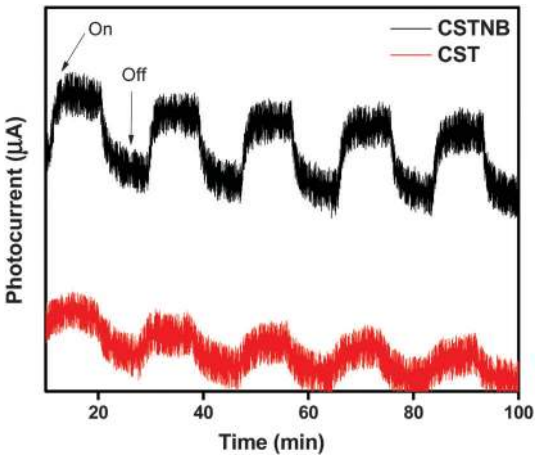

Fig. 8 Photoconductivity measurement of combustion synthesized TiO_2 and acid etched TiO_2 nanobelts.

cycles of light irradiation. The measured photocurrent was steady throughout the on and off cycles of light irradiation. The photocurrent response of TiO_2 nanobelts was higher compared to commercial TiO_2, indicating that the TiO_2 nanobelts utilize the illuminated light to the maximum extent. Even after switching off the light irradiation, the TiO_2 nanobelt sample exhibited residual current that could be due to trapped charges having extended life time.[49]

3.2. Catalysis

The photocatalytic performance of these materials was evaluated by degrading organic dye molecules under direct sunlight irradiation. Fig. 9(a) and (b) show the degradation profiles of anionic (methyl orange) and cationic (methylene blue) dyes with these catalysts and this is compared to standard commercial grade TiO_2, Degussa P-25. The blank experiments were conducted in the absence of sunlight, where the catalysts were experimented for their adsorption abilities. The as prepared combustion synthesized TiO_2 adsorbed around 15% of the initial concentration of methylene blue and methyl orange, respectively. The acid etched TiO_2 nanobelts and Degussa P-25 showed negligible dye adsorption. The photocatalytic efficiency of the as prepared combustion synthesized TiO_2 is similar to that of commercial TiO_2 for both the organic dyes. The acid etched TiO_2 nanobelts showed a much higher photocatalytic activity for both the dyes. The degradation of the dyes by the catalyst was analyzed by plotting C/C_0 with time.

$$\ln\left(\frac{C}{C_0}\right) = k_{app}t \qquad (2)$$

The above expression is the kinetic equation that governs the photocatalytic degradation, where C_0 and C are the initial concentration and final concentration of the dye at time 0 and t respectively. k is the apparent first order rate constant. $\ln(C/C_0)$ *versus* time was plotted to determine the k value from the slope. The k values of all the catalysts are tabulated in Table 1.

From the kinetic plot, as shown in Fig. 9(c) and (d), the rate constants obtained for acid etched TiO_2 nanobelts for both methylene blue ($(1257 \pm 3.0) \times 10^{-4}$ min^{-1}) and methyl orange ($(421.1 \pm 4.7) \times 10^{-4}$ min^{-1}) degradation were significantly higher compared to the rate constants of combustion synthesized TiO_2 and commercial TiO_2 indicating its superior photocatalytic activity.

The catalysts were also used to degrade methyl orange under an illuminated UV source. The degradation profile and kinetics of methyl orange photocatalysis are shown in Fig. 9(e) and (f). The rate of methyl orange degradation was slightly higher than the degradation rate under solar irradiation. This could be due to maximum spectral irradiance between 350 and 400 nm of light spectra where the band gap of catalysts exists and also only 2–5% of sunlight comprises UV light. Similarly, the photon energy of UV radiation from artificial lamps is higher than that of solar radiation. However, it has to be emphasized clearly that solar irradiation is abundant, sustainable, inexpensive and renewable. Hence, utilization of sunlight for catalysis is much favored. Similarly the photocatalytic activity of nanobelts derived from commercial Degussa P-25 was determined. The synthesized P25 nanobelts were also acid corroded. Both the P25 nanobelts and acid corroded P25 nanobelts were used to degrade methyl orange under solar irradiation and compared with acid etched combustion synthesized TiO_2 derived nanobelts. Fig. 9(g) shows the degradation profile of methyl orange using P25 nanobelts under solar radiation. It can be found that the photocatalytic degradation of the dyes by acid etched TiO_2 nanobelts was very higher compared to combustion synthesized TiO_2 and commercial TiO_2 nanoparticles and nanobelts. Efficient charge separation because of island – belt heterostructures and majority active phase exposure could be possible reasons for the enhanced photoactivity exhibited by acid etched TiO_2 nanobelts.

The nanobelts synthesized from P25 show a lower photocatalytic activity than pristine P25. This is because the surface area of P25 particles is 52 m^2 g^{-1} but it is 32 m^2 g^{-1} for P25 nanobelts. Furthermore, P25 particles form a thorough and good homogeneous dispersion in a dye solution compared to nanobelt structures. Therefore, better dispersion and higher surface area of P25 nanoparticles compared to P25 nanobelts contribute to its better photocatalytic activity.

3.2.1. Photocatalytic antimicrobial activity. The bacterial degradation experiments were performed under solar irradiation using commercial Degussa P-25, combustion synthesized TiO_2 and acid etched TiO_2 nanobelts. Control experiments were done without any catalyst particles in the bacterial suspension considering it as photolysis. Dark experiments were also conducted using the catalysts in the absence of sunlight. From Fig. 10, it is observed that acid etched TiO_2 nanobelts were efficient against degrading the microorganisms. It was reported that the reactive radical species generated by the catalyst was responsible for degrading the bacteria.[50] These hydroxyl radicals would attack the polyunsaturated phospholipid structure that is present in *E. coli*, which leads to the breakdown of the cell membrane and ultimate death of bacteria.[51,52]

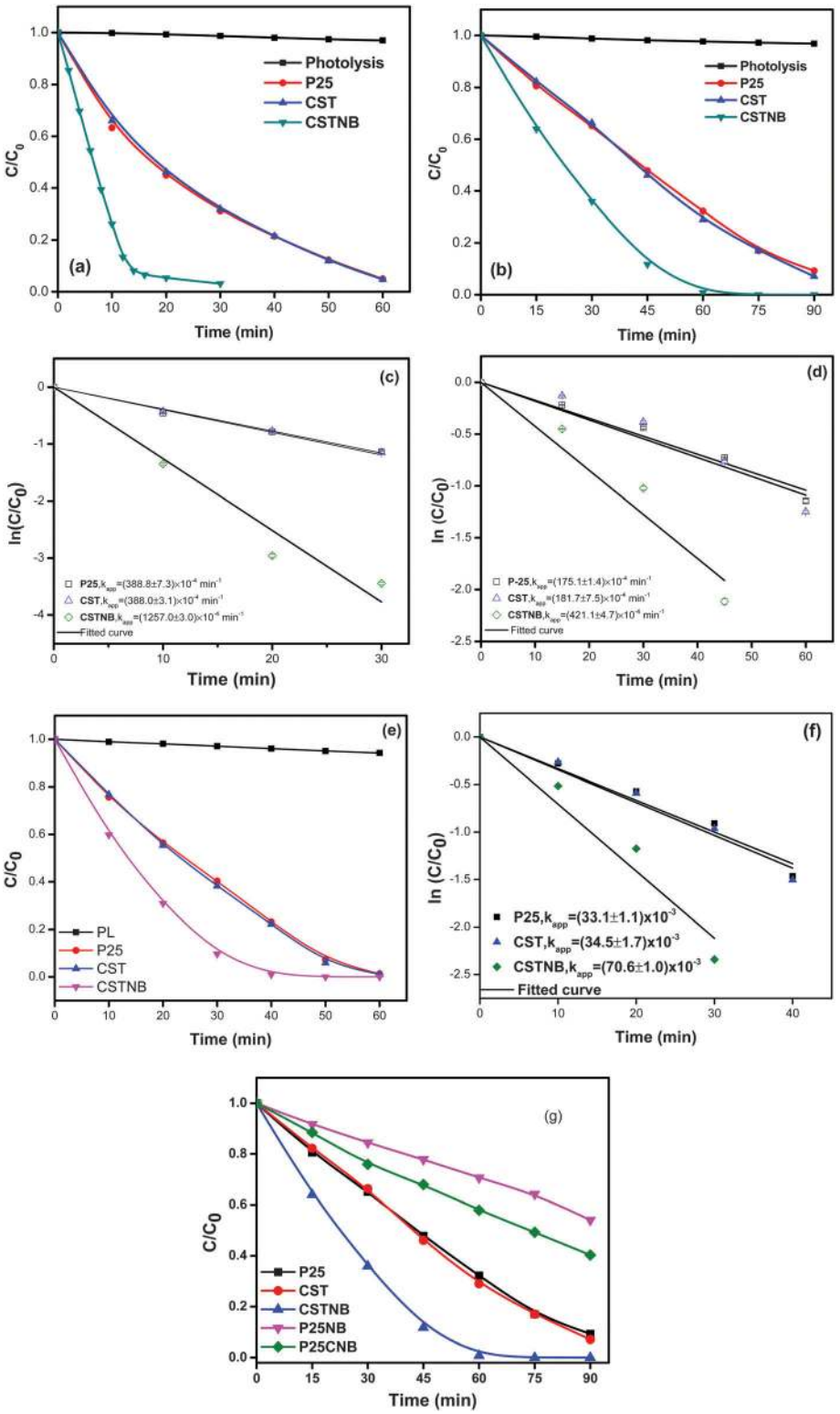

Fig. 9 (a) and (b) Photocatalytic degradation, (c) and (d) rate kinetics of methylene blue and methyl orange by combustion synthesized TiO_2, acid etched TiO_2 nanobelts and Degussa P-25 under solar irradiation. (e) and (f) Photocatalytic degradation of methyl orange under UV irradiation. (g) Photocatalytic degradation of methyl orange using P25 nanobelts and acid corroded P25 nanobelts under solar irradiation.

These hydroxyl radicals are capable of damaging the bacterial DNA.[53] Therefore, a large number of hydroxyl radicals generated by acid etched TiO_2 nanobelts could be responsible for its antibacterial activity. The bacterial degradation was very high initially up to 20 min and then decreases. This might be due to aggregation of dead bacterial cells upon live ones which

Table 1 Rate parameters for dye degradation and antibacterial activity of P-25, combustion synthesized TiO_2 and acid etched TiO_2 nanobelts under solar radiation

	Rate constant, k_{app} ($\times 10^{-4}$ min^{-1})		
Catalyst	Methylene blue	Methyl orange	*E. coli*[a]
Degussa P-25	388.8 ± 7.3	175.1 ± 1.4	641.7 ± 4.3
Combustion synthesized TiO_2	388 ± 3.1	181.7 ± 7.5	776.5 ± 34.3
Acid etched TiO_2 nanobelts	1257 ± 3.0	421.1 ± 4.7	1175 ± 24.4

[a] Unit of k for *E. coli* degradation is (CFU ml^{-1})$(1-n)$/min.

decreases their further degradation. The kinetics of bacterial degradation was determined using power law based kinetics

$$\frac{-\mathrm{d}C}{\mathrm{d}t} = kC^n, \tag{3}$$

The reaction rate constant is denoted as "k" (CFU ml^{-1})$(1-n)$/min, the plate count is denoted as "C" (CFU ml^{-1}) and the order of reaction is denoted as "n". Eqn (3) is solved to obtain,

$$\log\left(\frac{C}{C_0}\right) = \frac{\log\left\{1 + \left[(n-1)ktC_0^{(n-1)}\right]\right\}}{1-n} \tag{4}$$

The k and n values are calculated for bacterial degradation using various catalysts. It was shown that the order of the bacterial degradation reaction by TiO_2 can vary between 1.08 and 1.13 based on the choice of irradiation and amount of catalyst loading.[16,54] However, both the catalyst loading and irradiation were kept constant and the order was calculated accordingly. Fig. 7 shows the non-linear regression analysis of bacterial degradation data, the order of the reaction (n) was determined to be 1.1 for all degradation profiles and the corresponding rate constants were calculated. The rate constant of bacterial degradation using acid etched TiO_2 nanobelts is $((1175 \pm 24.4) \times 10^{-4})$ min^{-1}, which is significantly higher than that obtained using Degussa P-25 and combustion synthesized TiO_2, whose rate constants are $((641.7 \pm 4.3) \times 10^{-4})$ min^{-1} and $((776.7 \pm 34.3) \times 10^{-4})$ min^{-1} respectively.

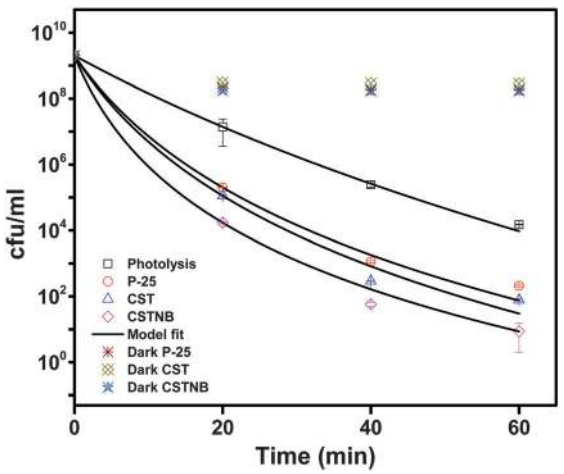

Fig. 10 Antibacterial activity of combustion synthesized TiO_2, acid etched TiO_2 nanobelts and Degussa P-25 against *E. coli* under solar irradiation.

3.2.2. Photocatalytic mechanism. The charge carrier mechanism of TiO_2 for photocatalysis has been well studied, where electrons and holes are generated upon shining light on the photocatalyst. These charges follow different pathways for producing hydroxyl radicals. However, charge trapping and carrier transportation that happens in the catalyst mostly determine the efficiency of photodegradation of contaminants.[55,56]

$$Ti^{IV} - OH^- + e_{CB}^- \rightarrow Ti^{III} - OH^- \text{ (Surface trap)} \tag{5}$$

$$Ti^{IV} + e_{CB}^- \rightarrow Ti^{III} \text{ (Deep trap)} \tag{6}$$

Even though the surface area of acid etched TiO_2 nanobelts is lower than that of combustion synthesized TiO_2, the photocatalytic activity is very high. Therefore, it can be suggested that the surface area alone cannot be responsible for higher activity but also other parameters like charge separation and crystal structure could be some of the reasons. The aspect ratio of the nano structures determines the effects on charge transport properties.[57] The TiO_2 nanoparticle interface with the nanobelt structure improves the photocatalytic activity for dye degradation.[29] Metal–nanostructure interfaces such as gold nanoparticles on top of ZnO nanorods[57] and gold on TiO_2 nanocomposites[58] have dramatically improved their photocatalytic activity. It has been reported that charge carriers could move along the length of the nanorod and then would efficiently separate at the interface between the nanoparticle and nanostructure. Therefore, based on the morphological aspect, the generated charge carriers of the TiO_2 particles can directly take part in the degradation process.[59] These particles over the acid etched TiO_2 nanobelts can accommodate trapping and separation of charge carriers excited from acid etched TiO_2 nanobelts or at the interface. These particles on top of each belt cause subtle difference in their valence band maxima such that excited charge carriers are easily separated by reducing the e^-/h^+ recombination at their interface. The presence of a large number of defects between etched particles and nanobelt surfaces can also decrease the recombination. The acid etched TiO_2 nanobelts have many voids which are retained by oxidation induced defects. These defects could help in reducing the charge recombination.

Facets and phase of the nano structure play a very important role in determining the property of a material. The faceted TiO_2 having an anatase phase exhibits superior photocatalytic activity.[60] There are many reports showing that the combination of anatase and rutile phases of TiO_2 exhibits superior catalytic activity compared to their individual phases. The exposure of the (101) plane of the anatase phase and the anatase to rutile ratio in the acid etched TiO_2 nanobelts is higher than the combustion synthesized TiO_2. This could be one of the reasons for the higher photocatalytic activity shown by acid etched TiO_2 nanobelts because combinations of anatase and rutile phases of TiO_2 have been proved to show a synergistic effect.[61] The presence of a rutile phase helps in transporting electrons to the anatase conduction band and leaving the holes behind reducing the carrier recombination. The rutile phase also extends the wavelength of light absorption[62,63] towards the visible region, which is observed in the case of combustion synthesized TiO_2 whose band gap is

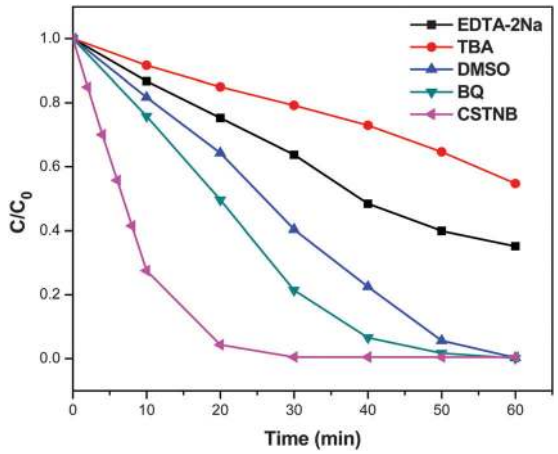

Fig. 11 Evaluation of reactive radical species using various scavengers for photocatalytic degradation of methylene blue by acid etched TiO_2 nanobelts.

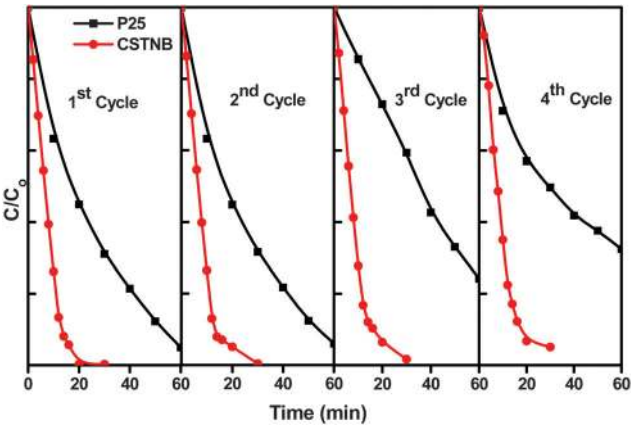

Fig. 12 Reusability of acid etched TiO_2 nanobelts compared against commercial Degussa P-25 for photocatalysis.

lower than that of other catalysts. The interface between small TiO_2 islands and the acid etched TiO_2 nanobelts, majority exposure of the active planes of the anatase phase, the aspect ratio of nano belt structures and combination of anatase and rutile, efficient charge transfer and maximum utilization of photons are responsible for the enhanced photocatalytic activity for dye degradation and antibacterial activity exhibited by acid etched TiO_2 nanobelts.

3.2.3. Scavenger reactions. In order to understand the reactive radical species that are responsible for efficient photocatalysis, a reaction of the photocatalytic reactant mixture with scavengers was carried out. Four different scavengers, EDTA-2Na$^+$ (hole scavenger),[64] tertiary-butyl alcohol ($^\bullet$OH scavenger),[65] DMSO (e^- scavenger),[66] benzoquinone ($O_2^{\bullet -}$ scavenger),[67] were mixed into the reactant mixture of methylene blue and catalyst particles and subjected to photocatalytic experiments under sunlight. Fig. 11 shows the photocatalytic response of acid etched TiO_2 nanobelts in the presence of scavengers. Since the band gap of TiO_2 nanobelts lies in the UV region, most of the reactive radicals responsible for catalytic activity are found to be photogenerated holes and hydroxyl radicals. However, it should also be noted that chemisorbed oxygen species on the TiO_2 nanobelts, which is confirmed from XPS analysis, can become superoxide radicals upon combining with photo-excited charge carriers. This is also found by adding benzoquinone which quenches superoxide species, and there is a decrease in the catalytic activity of acid etched TiO_2 nanobelts.

3.2.4. Reusability. The photostability of the catalysts was determined by reusing the catalysts for subsequent photodegradation experiments. The TiO_2 nanobelts and commercial TiO_2 were subjected to degradation of 20 ppm methylene blue under solar irradiation. After each experiment, the catalysts were separated by centrifugation of the reaction mixture and heat treatment at 100 °C for the subsequent cycle. From Fig. 12, it was found that the photoactivity of commercial TiO_2 has been reduced to 80% in the third cycle and to 60% during the fourth cycle compared to acid etched TiO_2 nanobelts, which have shown 98% and 96% degradation, respectively. Leaching of surfaces during the reaction attributing to loss of active sites and agglomeration of catalyst particles during heat treatment after every cycle could result in decreasing the photoactivity during reuse. However, the catalytic activity of acid etched TiO_2 nanobelts is consistent compared to that of commercial TiO_2.

4. Conclusions

The results from these studies demonstrate the utilization of natural sunlight as a source to degrade organic contaminants and inactivate harmful bacteria in the presence of combustion synthesized TiO_2 and acid etched TiO_2 nanobelts. TiO_2 nanoparticles were synthesized by a facile solution combustion technique using ascorbic acid as a fuel. Large surface area, red shift of diffused reflectance spectra and co-existence of both anatase and rutile phases have contributed to the high photocatalytic activity similar to that of commercial TiO_2. TiO_2 nanobelts were synthesized using combustion synthesized TiO_2 as a novel precursor. Unlike Degussa P-25, combustion synthesized TiO_2 as a precursor resulted in nanobelts with oxidation induced voids. Similarly, acid treatment of nanobelts resulted in the formation of partially etched belts and many small TiO_2 particle islands. The mechanism of formation of nanobelts was proposed. Acid etched TiO_2 nanobelts have shown enhanced photocatalytic activity than pristine combustion synthesized TiO_2, commercial Degussa P-25 and nanobelts synthesized from commercial TiO_2 for dye and bacterial degradation. The rate constants and order of the photocatalytic reactions were determined. Both dye and bacterial degradation by these catalysts have been ascertained to follow first order rate kinetics. Majority exposure of active planes of the anatase phase, combination of anatase and rutile phases, the aspect ratio of the nanobelt structure and effective charge transport between particle-island and belts have contributed to the enhanced photocatalytic activity. Evaluation of various reactive radical species responsible for high photoactivity was done using scavenger experiments. Formation of a large volume of holes and hydroxyl radical by the acid etched TiO_2 nanobelts upon irradiation using sunlight has caused

both organic dyes and bacteria to degrade rapidly. This study suggests that morphological tuning of nanobelts by utilizing various precursors of TiO_2 results in superior catalytic activity, and this can also be utilized as an effective substrate for active enhancement of light absorption by developing hybrid photocatalysts.

Acknowledgements

The authors thank Department of science and technology for financial support, Prof. Jayant Modak, Dept. of Chemical Engineering, IISc, for allowing us to perform microbial experiments, CeNSE and AFMM for characterization facilities. The authors thank Ms Disha Jain and Ms Leelavathi for assisting in XPS and TEM characterization.

References

1 A. Dufour, M. Snozzi, W. Koster, J. Bartram, E. Ronchi and L. Fewtrell, *Microbial safety of drinking water: Improving approaches and methods*, World Health Organization, 2003.
2 M. Pera-Titus, V. García-Molina, M. A. Baños, J. Giménez and S. Esplugas, *Appl. Catal., B*, 2004, **47**, 219–256.
3 J. Y. Kim, C. Lee, M. Cho and J. Yoon, *Water Res.*, 2008, **42**, 356–362.
4 K. P. Kühn, I. F. Chaberny, K. Massholder, M. Stickler, V. W. Benz, H.-G. Sonntag and L. Erdinger, *Chemosphere*, 2003, **53**, 71–77.
5 H. Lachheb, E. Puzenat, A. Houas, M. Ksibi, E. Elaloui, C. Guillard and J.-M. Herrmann, *Appl. Catal., B*, 2002, **39**, 75–90.
6 N. Miranda-García, M. I. Maldonado, J. Coronado and S. Malato, *Catal. Today*, 2010, **151**, 107–113.
7 D. Das and K. Parida, *Appl. Catal., A*, 2007, **324**, 1–8.
8 D. Das, N. Biswal, S. Martha and K. Parida, *J. Mol. Catal. A: Chem.*, 2011, **349**, 36–41.
9 M. K. Akhtar, S. E. Pratsinis and S. V. Mastrangelo, *J. Am. Ceram. Soc.*, 1992, **75**, 3408–3416.
10 S. T. Aruna, Solution Combustion Synthesis- An Overview, in *Combustion Synthesis: Novel routes to Novel Materials*, Bentham Science Publishers Ltd, 2010, pp. 206–221.
11 J. Yang, S. Mei and J. M. Ferreira, *J. Am. Ceram. Soc.*, 2000, **83**, 1361–1368.
12 J. Rubio, J. Oteo, M. Villegas and P. Duran, *J. Mater. Sci.*, 1997, **32**, 643–652.
13 L. Campbell, B. Na and E. Ko, *Chem. Mater.*, 1992, **4**, 1329–1333.
14 K. Nagaveni, M. Hegde, N. Ravishankar, G. Subbanna and G. Madras, *Langmuir*, 2004, **20**, 2900–2907.
15 G. Sivalingam, K. Nagaveni, M. Hegde and G. Madras, *Appl. Catal., B*, 2003, **45**, 23–38.
16 S. Sontakke, J. Modak and G. Madras, *Chem. Eng. J.*, 2010, **165**, 225–233.
17 C. Melendres, A. Narayanasamy, V. Maroni and R. Siegel, *J. Mater. Res.*, 1989, **4**, 1246–1250.
18 R. Akbarzadeh, S. B. Umbarkar, R. S. Sonawane, S. Takle and M. K. Dongare, *Appl. Catal., A*, 2010, **374**, 103–109.
19 A. Nezamzadeh-Ejhieh and S. Hushmandrad, *Appl. Catal., A*, 2010, **388**, 149–159.
20 M. Xing, J. Zhang and F. Chen, *Appl. Catal., B*, 2009, **89**, 563–569.
21 J. Schneider, M. Matsuoka, M. Takeuchi, J. Zhang, Y. Horiuchi, M. Anpo and D. W. Bahnemann, *Chem. Rev.*, 2014, **114**, 9919–9986.
22 M. Xing, X. Li and J. Zhang, *Sci. Rep.*, 2015, **5**, 8591.
23 B. Qiu, M. Xing and J. Zhang, *J. Am. Chem. Soc.*, 2014, **136**, 5852–5855.
24 L. G. Devi, S. G. Kumar, B. N. Murthy and N. Kottam, *Catal. Commun.*, 2009, **10**, 794–798.
25 L. G. Devi, N. Kottam, B. N. Murthy and S. G. Kumar, *J. Mol. Catal. A: Chem.*, 2010, **328**, 44–52.
26 N. Wu, J. Wang, D. N. Tafen, H. Wang, J.-G. Zheng, J. P. Lewis, X. Liu, S. S. Leonard and A. Manivannan, *J. Am. Chem. Soc.*, 2010, **132**, 6679–6685.
27 J. Wang, D. N. Tafen, J. P. Lewis, Z. Hong, A. Manivannan, M. Zhi, M. Li and N. Wu, *J. Am. Chem. Soc.*, 2009, **131**, 12290–12297.
28 M. Li, Y. Jiang, R. Ding, D. Song, H. Yu and Z. Chen, *J. Electron. Mater.*, 2013, **42**, 1290–1296.
29 W. Zhou, G. Du, P. Hu, G. Li, D. Wang, H. Liu, J. Wang, R. I. Boughton, D. Liu and H. Jiang, *J. Mater. Chem.*, 2011, **21**, 7937–7945.
30 Y. Wang, G. Du, H. Liu, D. Liu, S. Qin, N. Wang, C. Hu, X. Tao, J. Jiao and J. Wang, *Adv. Funct. Mater.*, 2008, **18**, 1131–1137.
31 W. Zeng, T. Liu and Z. Wang, *J. Mater. Chem.*, 2012, **22**, 3544–3548.
32 W. Zhou, H. Liu, J. Wang, D. Liu, G. Du and J. Cui, *ACS Appl. Mater. Interfaces*, 2010, **2**, 2385–2392.
33 A. D. Mani, P. M. K. Reddy, M. Srinivaas, P. Ghosal, N. Xanthopoulos and C. Subrahmanyam, *Mater. Res. Bull.*, 2015, **61**, 391–399.
34 T. Kasuga, M. Hiramatsu, A. Hoson, T. Sekino and K. Niihara, *Langmuir*, 1998, **14**, 3160–3163.
35 B. Yao, Y. Chan, X. Zhang, W. Zhang, Z. Yang and N. Wang, *Appl. Phys. Lett.*, 2003, **82**, 281–283.
36 Z.-Y. Yuan, J.-F. Colomer and B.-L. Su, *Chem. Phys. Lett.*, 2002, **363**, 362–366.
37 V. Bellat, R. Chassagnon, O. Heintz, L. Saviot, D. Vandroux and N. Millot, *Dalton Trans.*, 2015, **44**, 1150–1160.
38 L. Forss and M. Schubnell, *Appl. Phys. B: Photophys. Laser Chem.*, 1993, **56**, 363–366.
39 N. Serpone, D. Lawless and R. Khairutdinov, *J. Phys. Chem.*, 1995, **99**, 16646–16654.
40 H. Tang, H. Berger, P. Schmid, F. Levy and G. Burri, *Solid State Commun.*, 1993, **87**, 847–850.
41 L. Saraf, S. Patil, S. Ogale, S. Sainkar and S. Kshirsager, *Int. J. Mod. Phys. B*, 1998, **12**, 2635–2647.
42 G. Redmond, D. Fitzmaurice and M. Graetzel, *J. Phys. Chem.*, 1993, **97**, 6951–6954.
43 Z.-T. Wang, N. A. Deskins, M. A. Henderson and I. Lyubinetsky, *Phys. Rev. Lett.*, 2012, **109**, 266103.
44 L.-B. Xiong, J.-L. Li, B. Yang and Y. Yu, *J. Nanomater.*, 2012, **2012**, 9.

45 Y.-G. Zhang, L.-L. Ma, J.-L. Li and Y. Yu, *Environ. Sci. Technol.*, 2007, **41**, 6264–6269.
46 B. Santara, P. Giri, K. Imakita and M. Fujii, *J. Phys. Chem. C*, 2013, **117**, 23402–23411.
47 X.-G. Han, H.-Z. He, Q. Kuang, X. Zhou, X.-H. Zhang, T. Xu, Z.-X. Xie and L.-S. Zheng, *J. Phys. Chem. C*, 2008, **113**, 584–589.
48 J. Zheng, Q. Jiang and J. Lian, *Appl. Surf. Sci.*, 2011, **257**, 5083–5087.
49 J. Zhuang, S. Weng, W. Dai, P. Liu and Q. Liu, *J. Phys. Chem. C*, 2012, **116**, 25354–25361.
50 J. Kiwi and V. Nadtochenko, *Langmuir*, 2005, **21**, 4631–4641.
51 H. A. Foster, I. B. Ditta, S. Varghese and A. Steele, *Appl. Microbiol. Biotechnol.*, 2011, **90**, 1847–1868.
52 P.-C. Maness, S. Smolinski, D. M. Blake, Z. Huang, E. J. Wolfrum and W. A. Jacoby, *Appl. Environ. Microbiol.*, 1999, **65**, 4094–4098.
53 G. Gogniat and S. Dukan, *Appl. Environ. Microbiol.*, 2007, **73**, 7740–7743.
54 S. Sontakke, C. Mohan, J. Modak and G. Madras, *Chem. Eng. J.*, 2012, **189**, 101–107.
55 M. R. Hoffmann, S. T. Martin, W. Choi and D. W. Bahnemann, *Chem. Rev.*, 1995, **95**, 69–96.
56 A. L. Linsebigler, G. Lu and J. T. Yates Jr, *Chem. Rev.*, 1995, **95**, 735–758.
57 A. Leelavathi, G. Madras and N. Ravishankar, *Phys. Chem. Chem. Phys.*, 2013, **15**, 10795–10802.
58 V. Subramanian, E. Wolf and P. V. Kamat, *J. Phys. Chem. B*, 2001, **105**, 11439–11446.
59 R. Liu, P. Hu and S. Chen, *Appl. Surf. Sci.*, 2012, **258**, 9805–9809.
60 E. Grabowska, M. Diak, M. Marchelek and A. Zaleska, *Appl. Catal., B*, 2014, **156**, 213–235.
61 T. Ohno, K. Sarukawa, K. Tokieda and M. Matsumura, *J. Catal.*, 2001, **203**, 82–86.
62 G. Li and K. A. Gray, *Chem. Phys.*, 2007, **339**, 173–187.
63 D. C. Hurum, A. G. Agrios, K. A. Gray, T. Rajh and M. C. Thurnauer, *J. Phys. Chem. B*, 2003, **107**, 4545–4549.
64 H. Zhang, R. Zong and Y. Zhu, *J. Phys. Chem. C*, 2009, **113**, 4605–4611.
65 S. Yan, Z. Li and Z. Zou, *Langmuir*, 2010, **26**, 3894–3901.
66 D. Wang, Y. Duan, Q. Luo, X. Li, J. An, L. Bao and L. Shi, *J. Mater. Chem.*, 2012, **22**, 4847–4854.
67 W. Li, D. Li, S. Meng, W. Chen, X. Fu and Y. Shao, *Environ. Sci. Technol.*, 2011, **45**, 2987–2993.